Electronic Supplementary Information

Constructing a hierarchically structured $KNi_{0.67}Co_{0.33}PO_4 \cdot H_2O$-graphene hydrogel/Ni foam electrode for superior all-solid-state supercapacitor

Xueying Ma,[a] Hanfang Feng,[a] Tianxiang Yan,[a] Li Zhang*[a,b] Xuying Liu*[a,b] and Shaokui Cao*[a,b]

a School of Materials Science and Engineering, Zhengzhou University, Zhengzhou 450001, China

b Henan Key Laboratory of Advanced Nylon Materials and Application, School of Materials Science and Engineering, Zhengzhou University, Zhengzhou 450001, China

*Address correspondence to E-mail: lizhang9@zzu.edu.cn (L. Zhang), liuxy@zzu.edu.cn (X. Liu), and caoshaokui@zzu.edu.cn (S. Cao)

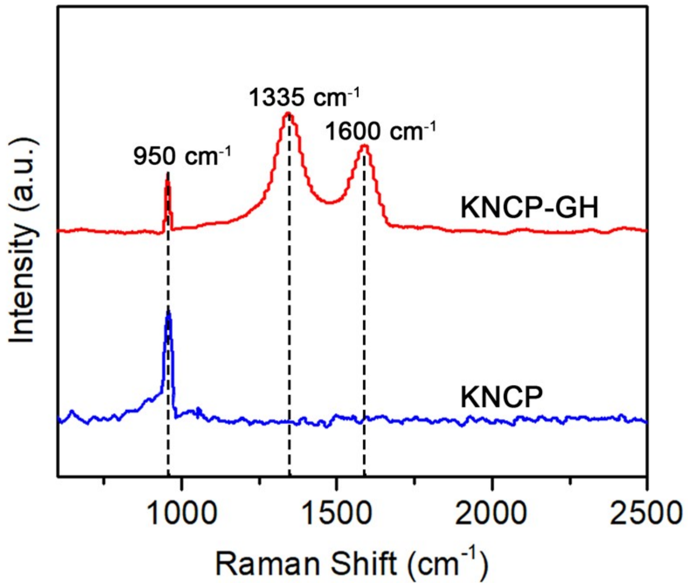

Fig. S1 Raman spectra of KNCP-GH and KNCP

Raman spectra was performed to substantiate the existence of GH in KNCP-GH composite. As shown in Fig. S1, the Raman spectrum of KNCP-GH presents three distinct bands. The first band at 950.0 cm^{-1} can be ascribed to the bending vibrations of PO_4^{3+} group in KNCP (with reference to the Raman spectrum of control sample KNCP).[S1] The other two bands at 1335 cm^{-1} and 1600 cm^{-1} can be attributed to the well-documented D and G bands of reduced GO respectively,[S2] confirming the existence of GH in KNCP-GH composite. Moreover, the D/G band intensity ratio of KNCP-GH composite, expressing the atomic ratio of sp^2/sp^3 carbon in GH, is calculated to be 1.38, which indicates a large quantity of structure defects in GH, also meaning the effective reduction of GO during hydrothermal process.[S3]

Table S1 The element contents based on XPS results of KNCP-GH

Element	C 1s	P 2p	K 2p	Ni 2p	Co 2p	O 1s
Atomic %	39.96	8.41	8.29	5.32	2.71	35.30

Table S2 ICP analysis results of KNCP-GH

Element	K	Ni	Co	P
Wt (%)	1.92	1.97	0.95	1.53
Atomic ratio	K : Ni : Co : P = 1 : 0.67 : 0.33 : 1			

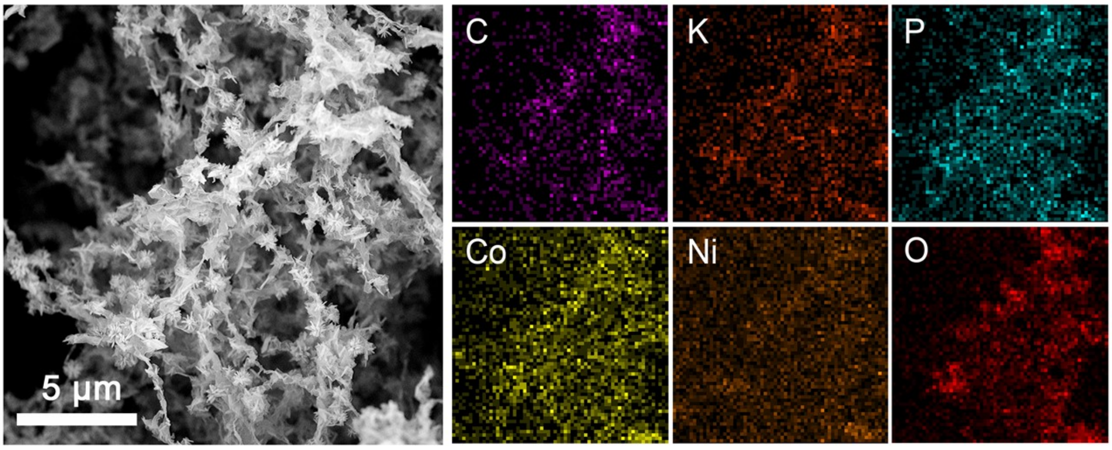

Fig. S2 EDS mapping images of C, K, P, Co, Ni and O elements of KNCP-GH/NF.

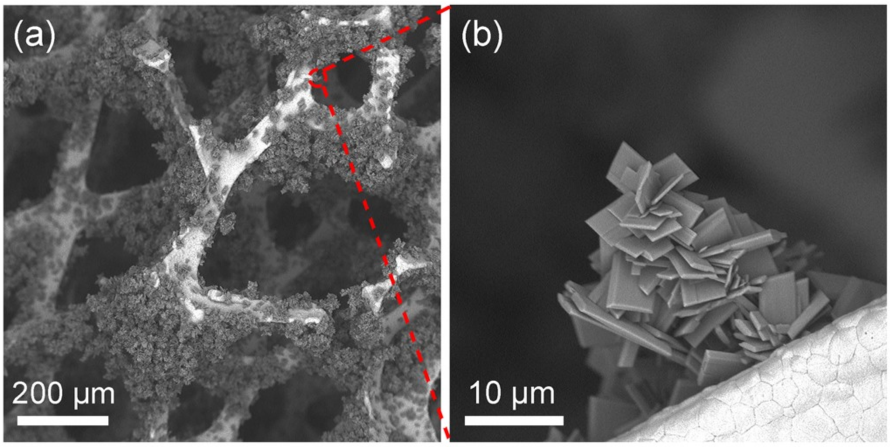

Fig. S3 SEM images of control sample KNCP/NF.

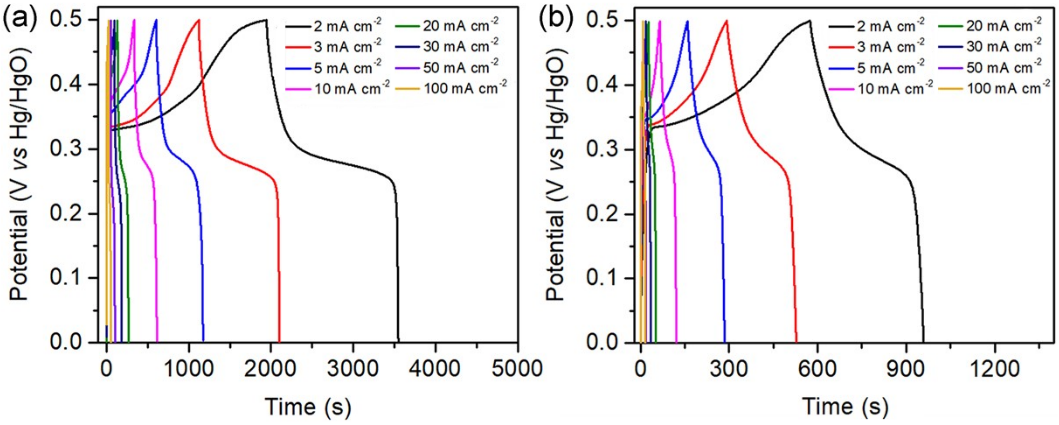

Fig. S4 GCD curves at different current densities for (a) KNCP-GH/NF and (b) KNCP/NF.

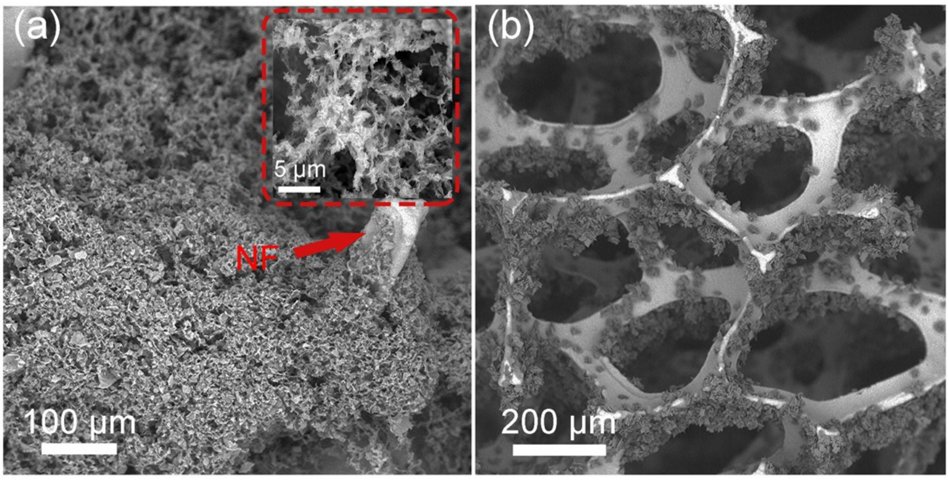

Fig. S5 SEM images of electrode after charge/discharge cycling tests at 50 mA cm^{-2}: (a) KNCP-GH/NF after 5000 cycles, (b) KNCP/NF after 2000 cycles.

Table S3 Comparison of electrode features (mass loading, particle size) and electrochemical properties of ATMP-based electrodes

Electrode	Mass Loading	Particle Size	Highest C (mF cm^{-2}/F g^{-1})	Capacitance retention	Ref.
$NH_4CoPO_4 \cdot H_2O$ microplate[*]	-	3~7 μm	-/369 at 0.625 A g^{-1}	82% at 6.25 A g^{-1}	S4
$NH_4CoPO_4 \cdot H_2O$ microbundles[*]	-	50 μm	3310/662 at 1.5 A g^{-1}	78% at 15 A g^{-1}	S5
$NH_4NiPO_4 \cdot H_2O$ plate@PPy/NF[**]	1.5 mg	5~10 μm	2269/1513 at 5 A g^{-1}	57% at 30 mA cm^{-2}	S6
$NH_4NiPO_4 \cdot H_2O$ nanoalmond[*]	-	350 nm	-/1072 at 1.5 A g^{-1}	62% at 13 A g^{-1}	S7
NH_4ZnPO_4 micropyramid/rGO[*]	-	2 μm	-/416 at 1 A g^{-1}	62% at 20 A g^{-1}	S8
KNiPO4 nanosheet[*]	-	2 μm	-/526 at 0.5 mA cm^{-2}	38% at 4 mA cm^{-2}	S9
NCNP[a]/rGO[*]	-	nanoscale	2979/993 at 0.5 A g^{-1}	81% at 32 A g^{-1}	S10
NCoNiP@NCoNiP[b] core-shell[*]	-	7 μm	-/1370 at 1 A g^{-1}	96% at 10 A g^{-1}	S11
Hybridized ATMP[c] microstructure[*]	-	10 μm	4060/1128 at 0.5 A g^{-1}	88% at 24 A g^{-1}	S12
NH_4-Ni-Co phosphate nanoslice[*]	-	nanoscale	5188/1297 at 0.5 A g^{-1}	89% at 24 A g^{-1}	S13
$NH_4(Ni,Co)PO_4$ microplate/rGO[*]	-	20 μm	-/1096 at 1 A g^{-1}	83% at 10 A g^{-1}	S14
$NH_4Co_xNi_{1-x}PO_4 \cdot H_2O$ microplate[*]	-	6~8 μm	5265/1567 at 1 A g^{-1}	81% at 20 A g^{-1}	S15
$KCo_{0.33}Ni_{0.67}PO_4 \cdot H_2O$ microplate[*]	-	10~20 μm	583/1166 at 1.5 A g^{-1}	66% at 30 A g^{-1}	S16
KNCP-GH/NF[**]	**3.7 mg**	**700 nm**	**6480/1751 at 2 mA cm^{-2}**	**78% at 100 mA cm^{-2}**	**this article**

*: powder-formed electrode; **: self-supported electrode;

a: $(NH_4)(Ni,Co)PO_4 \cdot 0.67\ H_2O$ microplates and $(Ni,Co)_3(PO_4)_2 \cdot 8H_2O$

b: $(NH_4)(Ni,Co)PO_4 \cdot 0.67\ H_2O$ nanosheets @single crystal microplatelets $(NH_4)(Ni,Co)PO_4 \cdot 0.67\ H_2O$

c: $(NH_4)(Ni,Co)PO_4 \cdot 0.67\ H_2O$ microplatelets and $(Ni,Co)_3(PO_4)_2$ nanoslice

Theoretical analysis on charge storage mechanism of electrode

The kinetic information obtained from CV curves can be used to identify the charge storage mechanism. From the theoretical point of view, the relationship between peak current i and scan rate ν follows the power law expressed as below:

$$i(V) = a\nu^b$$

Where a is a constant and b is the power-law exponent. The b-value can be determined from the slope of the plot of $\log i$ vs. $\log \nu$ for the anodic peaks, which provides insight regarding the charge storage mechanism. For a strictly diffusion-controlled redox reaction process, the peak current is proportional to the square root of the scan rate, thus $b = 0.5$; for a surface-confined capacitive process, the peak current has a linear relation with the scan rate, hence $b = 1$. Therefore, on the basis of the experimental b values, the kinetics of the charge storage mechanism can be determined qualitatively.

The contribution ratios of diffusion-controlled and surface capacitive processes to the total stored charge could be resolved under various scan rates via Dunn's method based on the following equation:

$$i(V) = k_1\nu + k_2\nu^{1/2}$$

Where $i(V)$ is the current response at the specific potential V, ν is the scan rate, and the terms $k_1\nu$ and $k_2\nu^{1/2}$ are the surface- and diffusion-controlled current components, respectively. This equation can be further transformed to:

$$i(V)/\nu^{1/2} = k_1\nu^{1/2} + k_2$$

The values of k_1 and k_2 are obtained from the slope and intercept of the $\nu^{1/2}$ vs.

$i(V)/v^{1/2}$ plot. These values are a quantitative indication of the capacitive and diffusive contributions to the total stored charge at a specific potential and given rate.

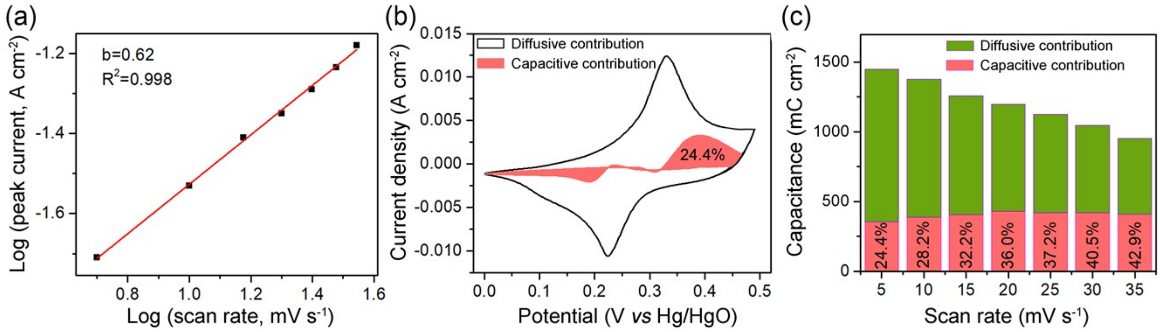

Fig. S6 (a) Determination of the b-value from the slope of log (peak current) vs. log (scan rate) plot based on the CV curves for KNCP/NF, (b) separation of the capacitive contribution (red shadow area) and diffusive contribution (blank area) to the CV currents at 5 mV s^{-1} for KNCP/NF, (c) capacitive and diffusive contribution ratios in the total stored charges at different scan rates for KNCP/NF electrode.

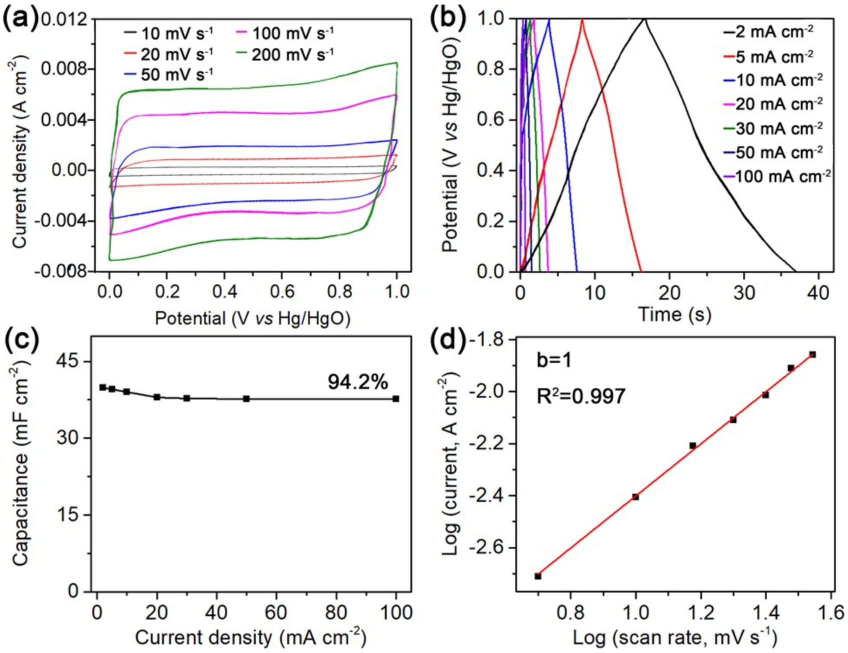

Fig. S7 (a) CV curves at various scan rates for GH/NF; (b) GCD curves of GH/NF; (c) rate performances of GH/NF; (d) Determination of the b-value from the slope of log (current) vs. log (scan rate) plot based on the CV curves for GH/NF.

The CV curves of GH/NF in Fig. S7a show a nearly rectangular shape, and the GCD curves of GH/NF in Fig. S7a assume a symmetric triangle shpae, which are specific to the EDL capacitive materials. The area-specific capacitances of GH/NF were calculated based on the GCD curves in Fig. S7b and are displayed in Fig. S7c. GH/NF exhibits the maximum area-specific capacitance of 40 mF cm^{-2}/ 199 F g^{-1} at 2 mA cm^{-2}, and still retains 94.2% of initial capacity when the current density is increased to 100 mA cm^{-2}, indicating its excellent rate performance. The calculated b-values are 1 for GH/NF, which indicates the surface-confined nature of GH/NF electrode.

Preparation of Fe_2P/graphene hydrogel/Ni foam composite (FGNF)

5 mL graphene oxide aqueous solution (2 mg mL^{-1}) and cleaned Ni foam were transferred into a 10 mL Teflon-lined autoclave and maintained at 180°C for 12 h to form a graphene hydrogel embedded with Ni foam (GH/NF). $FeCl_3$ (0.163 mg, 1 mmol) and urea (1.2 g, 20 mmol) were dissolved in 20 mL of water and stirred for 30 minutes to form a brown solution. Thereafter as-prepared GH/NF and the above solution were transferred into a 10 mL Teflon-lined autoclave, and the autoclave was sealed and maintained at 100°C for 6 h to obtain $Fe(OH)_3$/GH/NF. Finally, the precursor $Fe(OH)_3$/GH/NF mixed with NaH_2PO_2 (0.5 g, 5.6 mmol) were placed into a tube furnace and annealed at 300°C for 2 h at Ar atmosphere with a heating rate of 2°C min^{-1} to prepare Fe_2P/GH/NF (FGNF). The mass loading of active material (Fe_2P and GH) in FGNF is estimated to be 2.0 mg by the mass difference method.

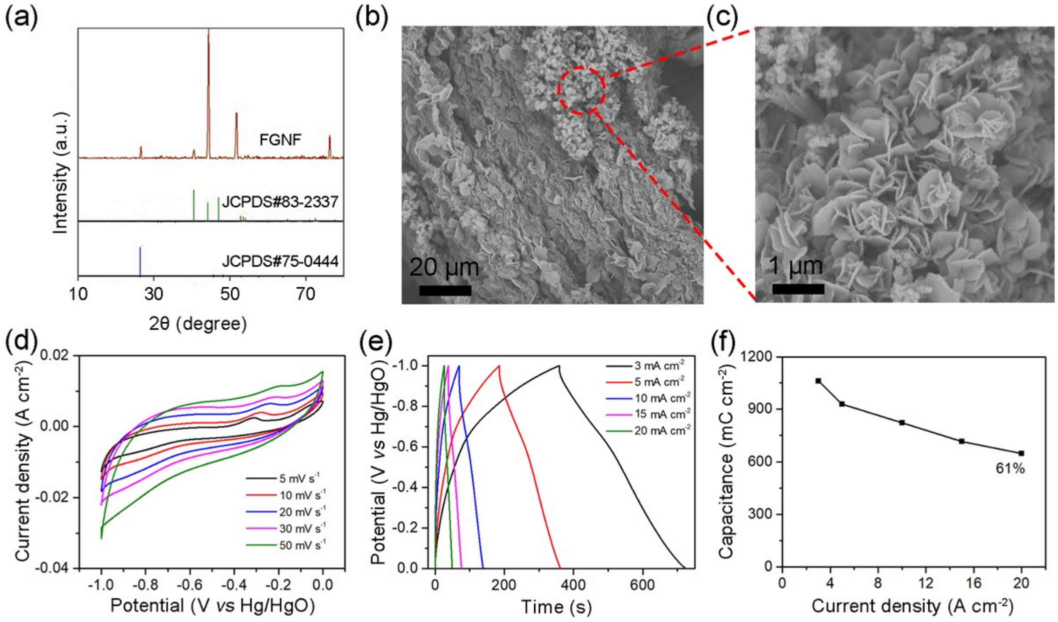

Fig. S8 Structure and electrochemical properties of FGNF: (a) XRD patterns, (b,c) SEM images, (d) CV curves at different scan rates, (e) GCD curves at different current densities, (f) rate performance.

The XRD pattern of FGNF is shown in Fig. S8a. The three salient peaks at 44.6°, 51.9° and 76.6° are ascribed to NF, and the 26.6° peak is originated from GH based on the standard diffraction patterns of graphitic carbon (JCPDS#75-0444), indicating the existence of graphene. The other well-defined three peaks at 40.5°, 51.9° and 54.2° can be indexed to Fe_2P according to the standard diffraction patterns (JCPDS#83-2337). The morphology of FGNF can be observed in the SEM images given in Fig. S8b and Fig. S8c, which show that small microflowers of Fe_2P with the contour size of ~1 μm grown on the surface of pore wall in graphene hydrogel, producing a Fe_2P/GH/NF hierarchical porous structure. Moreover, the electrochemical properties of FGNF was measured under a three-electrode system in 1 M KOH. As shown in Fig. S8d, the CV curves at various scan rates for FGNF manifest quasi-rectangular shapes accompanied by peaks at around -0.4 V, reflecting the existence of dominant pseudocapacitive nature within the potential window of -1~0V. Likewise, the symmetric and quasi-lined GCD curves at different current densities in Fig. S8e also verify the distinct pseudocapacitive characteristic. The area-specific capacitances of FGNF were calculated based on the GCD curves in Fig. S8e and are displayed in Fig. S8f. FGNF exhibits the maximum area-specific capacitance of 1060 mC cm^{-2} at 3 mA cm^{-2}, and still retains 61% of initial capacity when the current density is increased to 20 mA cm^{-2}, indicating its excellent capacitive properties.

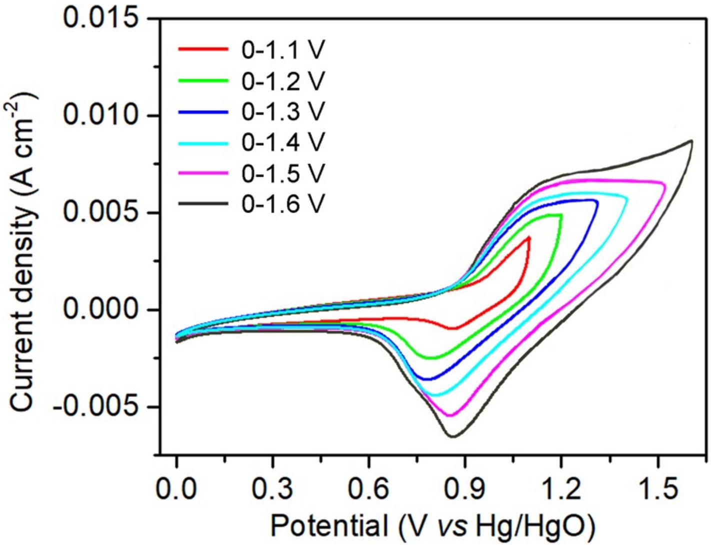

Fig. S9 CV curves of the KNCP-GH/NF//FGNF ASSSC at 2 mV s^{-1}.

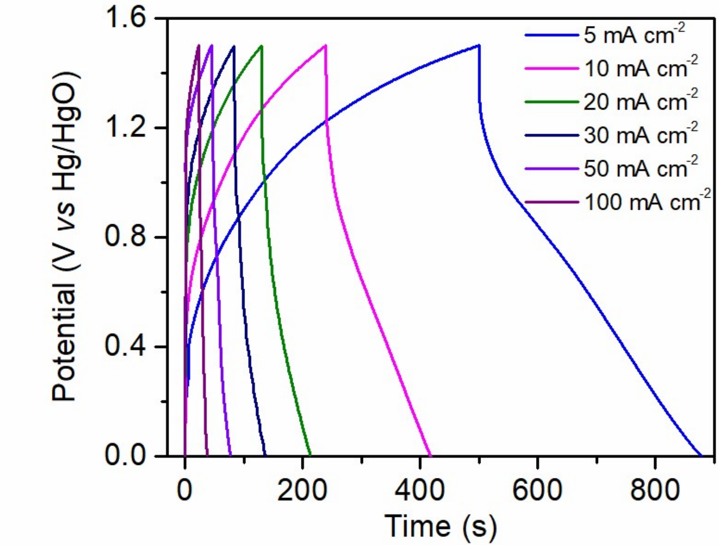

Fig. S10 GCD curves of KNCP-GH/NF//FGNF ASSSC.

Table S4 Comparison of energy/power densities of different asymmetrical supercapacitor related to ATMP

Positive material//Negative material	**Electrolyte**	**Maximum energy density （Wh kg^{-1}/mWh cm^{-3}）**	**Maximum power density （W kg^{-1}/mW cm^{-3}）**	**Ref.**
$NH_4CoPO_4\cdot H_2O$//graphene nanosheets	3 M KOH	26.6/-	7000/-	S5
$NH_4NiPO_4\cdot H_2O$@PPy/NF//AC	3 M KOH	41.6/-	8500/-	S6
NH_4ZnPO_4/rGO//rGO	3 M H_2SO4	59.9/-	8935/-	S8
$KNiPO_4$//AC	1 M KOH	13/-	678/-	S9
NCNP/rGO//HPC	6 M KOH	42.1/2.35	14000/896	S10
NCoNiP@NCoNiP//HPC	6 M KOH	44.5/2.66	7400/465	S11
Hybridized ATMP//HPC	6 M KOH	35.3/-	4400/-	S12
NH_4-Ni-Co phosphate//HPC	6 M KOH	38.4/-	11041/-	S13
$NH_4Co_xNi_{1-x}PO_4\cdot H_2O$//AC	3 M KOH	37.4/3.36	12400/743	S15
$KCo_{0.33}Ni_{0.67}PO_4\cdot H_2O$ //AC	1 M KOH	80.6/2.02	8000/200	S16
$NaNi_{0.33}Co_{0.67}PO_4\cdot H_2O$//graphene	1 M KOH	29.9/0.90	7500/900	S17
KNCP-GH/NF//FGNF	**PVA-KOH(1 M)**	**69.2/3.95**	**13229/720**	**this article**

REFERENCE:

S1 C. Foo, H. Lim, M. Mahdi, K. Chong, N. Huang, *J. Phys. Chem. C,* 2016, 120, 21202-21210.

S2 S. Gao, L. Zhang, Y. Qiao, P. Dong, J. Shi, S. Cao, *RSC Adv.*, 2016, 6, 58854-58861.

S3 J. Chen, K. Sheng, P. Luo, C. Li, G. Shi, *Adv. Mater.*, 2012, 24, 4569-4573.

S4 H. Pang, Z. Yan, W. Wang, J. Chen, J. Zhang, H. Zheng, *Nanoscale*, 2012, 4, 5946-5953.

S5 S. Wang, H. Pang, S. Zhao, W. Shao, N. Zhang, J. Zhang, J. Chen, S. Li, *RSC Adv.*, 2014, 4, 340-347.

S6 C. Chen, N. Zhang, X. Liu, Y. He, H. Wan, B. Liang, R. Ma, A. Pan, V. Roy, *ACS Sustain. Chem. Eng.*, 2016, 4, 5578-5584.

S7 J. Zhao, H. Pang, J. Deng, Y. Ma, B. Yan, X. Li, S. Li, J. Chen, W. Wang, *CrystEngComm*, 2013, 15, 5950-5955.

S8 T. Raja, P. Vickraman, A. Justin, B. Reddy, *Phys. Status Solidi A-Appl. Mat.,* 2019, 217, 1900736-1900746.

S9 N. Priyadharsini, R. Selvan, *Electrochim. Acta*, 2017, 246, 963-970.

S10 M. Wang, F. Jin, X. Zhang, J. Wang, S. Huang, X. Zhang, S. Mu, Y. Zhao, Y. Zhao, *ACS Sustain. Chem. Eng.*, 2017, 5, 5679-5685.

S11 M. Wang, Y. Zhao, X. Zhang, R. Qi, S. Shi, Z. Li, Q. Wang, Y. Zhao, *Electrochim. Acta*, 2018, 272, 184-191.

S12 Z. Chen, D. Xiong, X. Zhang, H. Ma, M. Xia, Y. Zhao, *Nanoscale*, 2016, 8, 6636-6645.

S13 Y. Zhao, Z. Chen, D. Xiong, Y. Qiao, Y. Tang, F. Gao, *Sci. Rep.*, 2016, 6, 17613.

S14 S. Zhang, H. Gao, J. Zhou, *J. Alloy. Compd.*, 2018, 746, 549-556.

S15 Q. Li, Y. Li, H. Peng, X. Cui, M. Zhou, K. Feng, P. Xiao, *J. Mater. Sci.*, 2016, 51, 9946-9957.

S16 B. Liang, Y. Chen, J. He, C. Chen, W. Liu, Y. He, X. Liu, N. Zhang, V. Roy, *ACS Appl. Mater. Interfaces*, 2018, 10, 3506-3514.

S17 M. Liu, N. Shang, X. Zhang, S. Gao, C. Wang, Z. Wang, *J. Alloy. Compd.*, 2019, 791, 929-935.